

Plasma-Assisted Synthesis of Carbon Nanotubes from Naturally Occurring Catalysts in Floral Biomass for Ultrafast Lithium/Sodium-Ion Batteries

Prashant S. Misal, Suyog A. Raut, Ujjwala P. Chothe, Ramchandra S. Kalubarme, Vikas L. Mathe, Damien Thiry, Milind V. Kulkarni, Sharmila R. Chaudhari,* and Bharat B. Kale*

This study highlights the synthesis of open-ended carbon nanotubes (CNTs) and disordered amorphous carbon using a plasma-based approach. The unique combination of open-ended CNTs and disordered carbon contributes to exceptional anode performance for lithium-ion (LIB) and sodium-ion batteries (SIB). Field-emission scanning electron microscopy images confirm the presence of CNTs intertwined with porous carbon, while transmission electron microscopy analysis reveals CNTs with an average diameter of 85 nm. The selected area electron diffraction pattern indicates an interlayer D-spacing of 0.35 nm, characteristic of disordered carbon. As an anode for LIBs, the material delivers an initial capacity of 394 mAh/g at 0.05 A/g and maintains

233 mAh/g after 3000 cycles at 1.5 A/g. Meanwhile, for SIB, it is assessed at a high current rate of 0.5 A/g, where it exhibits that the specific capacity remains steady at around 75 mAh/g over 5000 cycles. The synergistic structure of CNTs and disordered carbon enhances ion transport and provides abundant active sites for Na⁺ and Li⁺ intercalation. The increased interlayer spacing, porous morphology, and interconnected structure reduce ion diffusion resistance, enabling superior rate performance. The sustainable plasma synthesis method, combined with high capacity, long cycle life, and versatility in LIBs and SIBs, makes it a promising candidate for next-generation energy storage.

1. Introduction

The swift expansion of global economies, driven by breakthroughs in technological sectors and industries, has resulted in an escalating demand for energy resources.^[1] The continual rise in global population and modern societal development further amplifies this demand. Conventional energy sources, primarily fossil fuels, coal, and petroleum, are being consumed at unprecedented rates, raising serious concerns about resource depletion and escalating environmental degradation.^[2] There is an urgent need to transition to sustainable, eco-friendly energy

solutions as the depletion of these finite resources approaches critical levels.^[3–5] The advancement of carbon materials derived from biomass holds great potential. Carbon materials are becoming integral to the advancement of high-performance energy storage systems, including lithium-ion batteries (LIBs), sodium-ion batteries (SIBs), and supercapacitors (SCs), as the global energy panorama shifts toward renewable resources.^[6,7]

Biomass-derived carbon offers an abundant, sustainable, and environmentally friendly alternative to conventionally synthesized carbons. Carbon materials, particularly those obtained from biomass, are drawing significant attention due to their unique characteristics, including structural stability, superior electrical conductivity, and flexible porosity.^[8,9] These characteristics make biomass-derived carbons particularly beneficial for energy storage applications. Recently, researchers have investigated a range of biomass precursors, including cotton rose,^[10] *Salvia splendens*,^[11] peanut shells,^[12] pinecone,^[13] *Camellia oleifera* shells,^[14] cherry flowers,^[15] mangosteen shells,^[16] lotus stems,^[17] date palms,^[18] banana stem,^[19] and orange peel.^[20] These naturally occurring sources have yielded carbon materials that exhibit high energy densities, stable long-term performance, and extended cycle life, making them viable electrode materials for LIBs, SIBs, and SCs.^[21]

A more recent and impactful development in the field of nanomaterials is the synthesis of CNTs from biomass. Traditionally, CNTs were produced using expensive precursors such as methane or acetylene through chemical vapor deposition (CVD), which posed significant economic and environmental challenges.^[22,23] The introduction of biomass as a source material for CNT synthesis represents a crucial advancement toward


P. S. Misal, S. R. Chaudhari
Baburaoji Gholap College Sangvi
Pune 411027, India
E-mail: shar_chaudhari@yahoo.co.in

P. S. Misal, S. A. Raut, R. S. Kalubarme, M. V. Kulkarni, B. B. Kale
Centre for Materials for Electronics Technology (C-MET)
Pune 411008, India
E-mail: bbkale1@gmail.com

S. A. Raut, D. Thiry
Chimie des Interactions Plasma-Surface (ChIPS)
Université de Mons
20 Place du Parc, Mons B-7000, Belgium

U. P. Chothe, B. B. Kale
Dr. Vishwanath Karad MIT World Peace University
Paud Rd, Kothrud, Pune 411038, India

V. L. Mathe
Savitribai Phule Pune University
Pune, Maharashtra 411007, India

 Supporting information for this article is available on the WWW under <https://doi.org/10.1002/batt.202500203>

sustainability, offering an ecologically responsible and lucrative alternative. Biomass-derived CNTs have attracted considerable attention owing to their ability to reduce both the financial and ecological footprint associated with conventional CNT production methods.^[24] Furthermore, many biomass materials contain natural catalytic elements, such as iron,^[25] cobalt, nickel, etc. which facilitate CNT growth.^[26] This directly minimizes the need for additional, often costly, catalysts. This paradigm shift in CNT production aligns with broader trends in nanomaterial research, which increasingly emphasize sustainable practices and green chemistry. By leveraging abundant and renewable biomass sources, researchers can develop innovative CNT synthesis techniques that not only enhance performance but also mitigate environmental impact. As the field progresses, optimizing these synthesis methods for yield and quality will be of prime importance, positioning biomass-derived CNTs as a mainstay in the advancement of electronic devices and next-generation energy storage. These advancements have the potential to make a substantial contribution to the global shift toward transitioning to a more sustainable energy landscape.

This study uses a DC thermal plasma reactor to present a novel one-step synthesis method for producing biomass-derived carbon nanotubes (CNTs) from Royal Poinciana (RP, *Delonix regia*) flowers. These flowers, known locally in India as Gulmohar, bloom abundantly during the spring, making them an ideal and renewable source of biomass. The RP flower is particularly intriguing due to its inherent iron content, which serves as a natural catalyst for CNT formation, thereby eliminating the need for additional catalyst materials typically required in conventional CNT synthesis methods. This simplification not only enhances the sustainability of the overall approach but also contributes to the economic viability of biomass-derived CNT production. Furthermore, advancements in processing techniques, such as plasma treatments, have enabled the high-yield and high-purity extraction of CNTs from biomass, opening new frontiers for their applications in energy storage. The synthesized CNTs were systematically characterized and evaluated for their electrochemical performance in LIB and SIB applications, with preliminary results indicating a promising combination of high energy density, exceptional cycle stability,

and cycle-long life. These findings suggest that biomass-derived CNTs can be crucial in driving the progress of energy storage technologies, particularly as sustainable alternatives to synthetic carbon-based materials. This research underscores the potential of utilizing renewable biomass resources to resolve the challenges linked to energy storage and sustainability.

2. Experimental Section

2.1. Synthesis of Floral-Based CNTs

RP flowers were collected from a home garden. The material was meticulously washed with distilled water to ensure the removal of impurities and then dried at 120 °C to effectively eliminate any residual moisture, ensuring optimal conditions for subsequent processes. The dried flowers were pulverized into a fine powder and calcined in a thermal arc plasma reactor under an N₂ atmosphere for 10 min. Operating conditions included a pressure of 350 Torr (base pressure of 10–3 Torr), an arc current of 150 A, and an arc voltage of 50 V, achieving a reaction temperature of ≈5000 K. Postcalcination, the powder was treated with HNO₃ to remove metal impurities; it was then rinsed with distilled water and ethanol, followed by drying for 12 h. The final sample was designated as RP.

The direct current transferred arc thermal plasma reactor (DCTATPR) used in biomass processing is also a highly versatile tool for producing nanomaterials of metals,^[27] alloys,^[28,29] and metal oxides.^[30] The details of the DCTATP reactor are discussed elsewhere. A unique high-density graphite crucible was designed to facilitate high efficiency through reduced thermal loss and to process the biomass at temperatures above 5000 K. The graphite cylinder, having a diameter of 50 mm, was machined to produce the crucible with two cross grooves at the bottom center, creating four touch points to the anode, and a lid with a few holes drilled. The holes are drilled into the lid and the crucible to facilitate the exit of the syngases produced during plasma pyrolysis. The plasma pyrolysis process is immaculate and rapid, with low or no byproducts. **Figure 1a** shows the schematic of DCTATPR, and

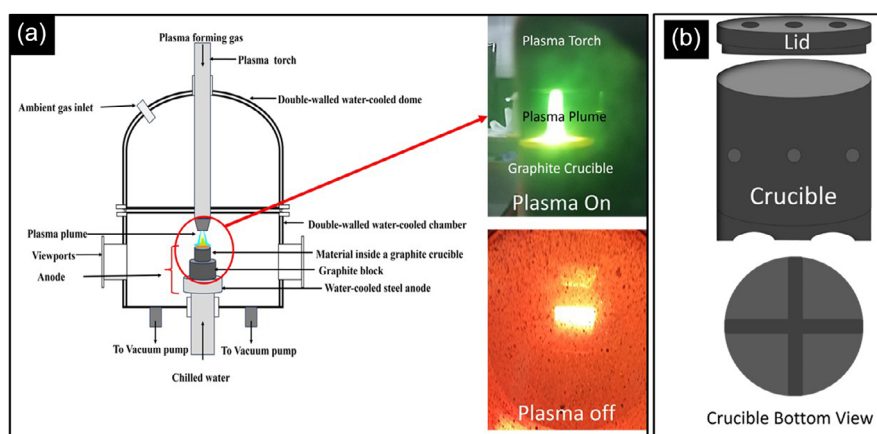


Figure 1. a) Schematic of DCTATP reactor showing an actual photograph of plasma plume (on and off state) and b) graphite crucible design.

the plasma plume impinging on the graphite crucible containing the biomass. Figure 1b shows the design of the high-density graphite crucible used to hold and pyrolyze the material inside the plasma reactor.

The dried biomass powder is compressed into a pellet using a hydraulic press and placed inside a custom-designed graphite crucible with a securely fitted lid. The crucible is then positioned inside the plasma reactor, resting on a steel anode that is protected by an additional graphite block to prevent damage from electrical arcs. Once the reactor is sealed, it is evacuated to a base pressure of 10^{-3} Torr. Next, the reactor is filled with nitrogen or argon gas to an operating pressure of 350 Torr. The plasma is ignited, and the heating process is conducted for 10 min. Afterward, the reactor and the material are allowed to cool for 30 min before the material is collected for further processing and analysis.

2.2. Preparation of Electrodes

Acetylene black (Global Nanotech, India) and N-methyl-2-pyrrolidone (NMP) (SD Fine Chemicals) were utilized in electrode preparation. The as-prepared carbon sample, polyvinylidene fluoride (PVDF), and acetylene black were mixed in a mass ratio of 8:1:1, with NMP serving as the solvent to form a homogeneous slurry. Copper and aluminum foils, cleaned with acetone and absolute ethanol, were used as current collectors. For LIB applications, the prepared slurry was uniformly coated onto copper foil, while for SIBs, the slurry was coated onto aluminum foil and dried at 100 °C. Electrodes were punched into 16 mm diameter disks for use in half-cell coin cell assemblies (CR2032).

For the LIB half-cell, lithium foil served as the counter electrode, with the coated carbon on copper foil acting as the working electrode (anode). A LiPF_6 -based electrolyte was employed to facilitate lithium-ion transport, and the assembled cell was designated as RPLi. For SIB half-cells, sodium foil was used as the counter electrode, with the prepared carbon coated on aluminum foil serving as the anode. 1M NaPF_6 in diglyme was selected as the electrolyte for Na-ion transfer, and the resulting cell was designated as RPNa.

2.3. Electrochemical Measurements

Electrochemical impedance spectroscopy (EIS) and cyclic voltammetry (CV) measurements were conducted on an IVM electrochemical workstation. EIS was performed within a frequency range of 0.1 to 1e^5 Hz at open-circuit voltage, with an alternating current amplitude of 5 mV. CV measurements were conducted within a voltage window of 0.01–3.0 V at a scan rate of 0.1 mV/s. The charge–discharge performance was evaluated over a potential range of 0.01–3.0 V using a Neware battery tester at various current densities.

2.4. Material Characterization

The structure of the sample was characterized using a Bruker D8 Advance X-ray diffractometer with Cu target $\text{K}\alpha$ ray under an acceleration voltage of 40 kV and an acceleration current of 40 mA. Raman spectra were obtained by Renishaw In Via Raman spectroscopy using a 532 nm Argon laser light source. The X-ray photoelectron spectroscopy (XPS) experiments used a surface analysis system (ThermoFisher Escalab Xi⁺). The $\text{AlK}\alpha$ radiation of the X-ray source is $h\nu = 1486.6$ eV. The binding energy was corrected by setting the $\text{C}1\text{s}$ peak to 284.8 eV, and then fitting the $\text{C}1\text{s}$. The morphology of the samples was observed by Hitachi S4800 field emission scanning electron microscopy (FE-SEM). FE transmission electron microscopy (FE-TEM) was recorded on a JEOL JEM-2200FS transmission electron microscope. Elemental analysis was conducted using an ICP-OES (Agilent Technologies 725) system to determine the elemental composition of the samples.

3. Result and Discussion

3.1. X-Ray Diffraction

As shown in Figure 2a, the XRD pattern exhibits broad peaks at 25° and 43° , indicating that the sample has low crystallinity and is mostly amorphous. The peak around 25° is attributed to the (002)

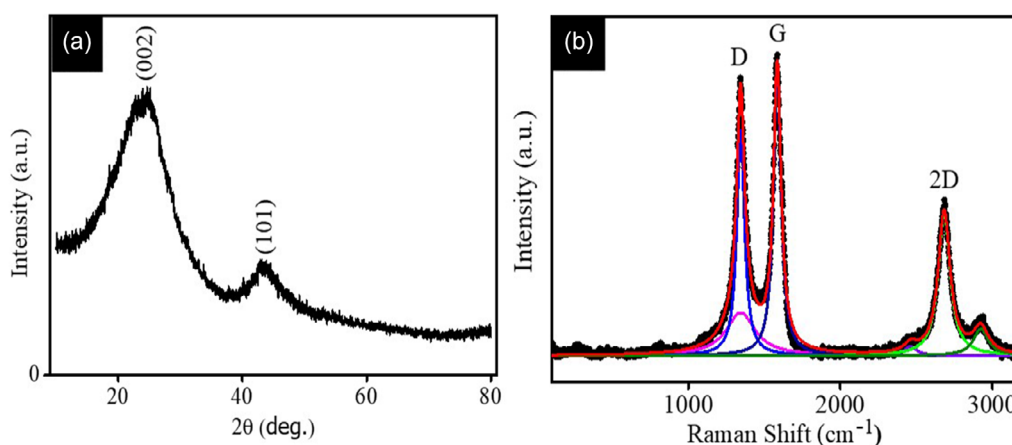


Figure 2. a) XRD pattern and b) Raman spectra of RP sample.

plane of graphitic carbon, but its broadness suggests that the carbon layers are disordered compared to graphitic carbon (JCPDS No. 00-002-0456), lacking long-range order.^[31] The peak around 43° is related to the (101) plane of carbon, reflecting the in-plane structure of the carbon atoms, but again, the broad peak indicates a disordered structure.^[32] The characteristic XRD peaks for CNTs, specifically the (002) and (101) planes, also appear around 25° and 43°. Additionally, CNTs are present in low concentrations within the amorphous carbon matrix; their signals in the XRD pattern might be too weak due to the merging of CNT peaks.

3.2. Raman Spectroscopy

Figure 2b shows RP's deconvoluted Raman spectra, and the peak around 1350 cm⁻¹ corresponds to the D-band. The D-band indicates disorder or defects in the carbon structure, commonly associated with amorphous carbon or defects in CNTs. The carbon material was processed at high temperatures in a thermal plasma reactor, where the presence of CNTs was confirmed by FESEM and TEM images. The observed D-band indicates imperfections or defects, which could exist within the CNTs or surrounding amorphous carbon regions.

The peak around 1580 cm⁻¹ is attributed to the G-band, which reflects the in-plane vibration of sp²-hybridized carbon atoms within graphitic materials. A strong G-band signifies a graphitic structure in the sample, confirming the presence of graphitized carbon and possibly well-developed CNTs.^[33] The intensity ratio of the D-band to the G-band (I_d/I_g) is crucial in understanding the degree of disorder or graphitization in carbon material. From Figure 2b, the ratio I_d/I_g is 0.85, which implies the material contains a mix of amorphous and graphitic carbon, which reflects a moderate degree of graphitic ordering alongside structural defects. This ratio suggests that the carbon framework has ordered graphitic (CNTs) domains conducive to electron transport and defect-rich amorphous regions, creating more active sites for ion storage.^[34] The peak is centered around 2700 cm⁻¹, corresponding to the 2D band (or G' band). This band is important for assessing the CNTs' quality and the graphene layers' stacking.^[35] A broad and less intense 2D-band compared to the G-band suggests the presence of multiwalled CNTs (MWCNTs).^[36]

3.3. XPS

The RP sample's surface chemical composition and bonding environments were examined using XPS. In the high-resolution C1s spectrum from Figure 3a, peaks were deconvoluted at 284.4, 285.5, 287.3, and 289.3 eV. The peak observed at 284.4 eV is for C–C, which is attributed to the graphitic structure, and the peak at 285.8 eV is associated with structural defects, reflecting disordered carbon atoms.^[37–40]

Additionally, the 287.3 and 289.7 eV peaks are attributed to oxygen-containing groups such as C–O and O–C=O, respectively.^[41] These features highlight the amorphous nature of carbon and the defects in CNTs arising from surface oxidation. The presence of these chemical states confirms the incorporation of heteroatom-functional groups on the sample's surface. Deconvolution of the XPS O 1s peak (Figure 3b) revealed the presence of carbonyl and hydroxyl functional groups on the surface. The peak at 533.2 eV corresponds to the C–O–C, C–O–OH, and C–OH groups, while the peak at 532.5 and 534.1 eV is associated with the C=O and O–C=O groups, respectively.^[40,42]

These oxygen-containing functionalities suggest mild surface oxidation, improving electrolyte wettability and interfacial compatibility, albeit with a slight reduction in electronic conductivity. Overall, the XPS analysis highlights the hybrid nature of the sample, where CNTs provide conductive sp²-rich regions, and amorphous carbon contributes sp³-rich domains, making the material highly suitable for electrochemical applications.

3.4. ICP-AES

Inductively coupled plasma (ICP) analysis was conducted to evaluate the elemental composition of biomass-derived carbon from the RP flower powder, dried at 100 °C, and subsequently after acid leaching. From Table 1, the ICP results of the RP flower powder before plasma treatment revealed substantial concentrations of manganese (Mn) at 6144.3 ppm and iron (Fe) at 1683.3 ppm, with cobalt (Co) detected at 22.4 ppm and boron (B) undetectable. The acid leaching aimed to reduce metal impurities; Mn and Fe levels significantly decreased to 10 ppm and 87.2 ppm, respectively, while Co and B remained undetectable. This acid-leaching step effectively minimized the metal content in the sample,

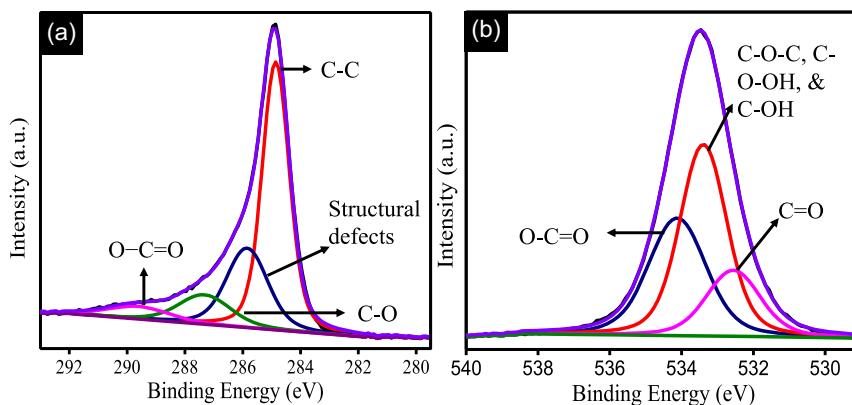


Figure 3. a) C1s and b) O1s XPS spectra of RP.

Table 1. ICP analysis of the RP sample.

	Elements (in ppm)			
	Co	Fe	Mn	B
RP flower dried powder at 100 °C	22.4	1683.3	6144.3	ND
Acid leaching after the plasma process	ND	87.2	10	ND

(ND- not detected).

particularly for Mn and Fe, which are generally present in biomass and can impact the structural and electrochemical properties of carbon materials in energy storage applications.

3.5. FE-SEM

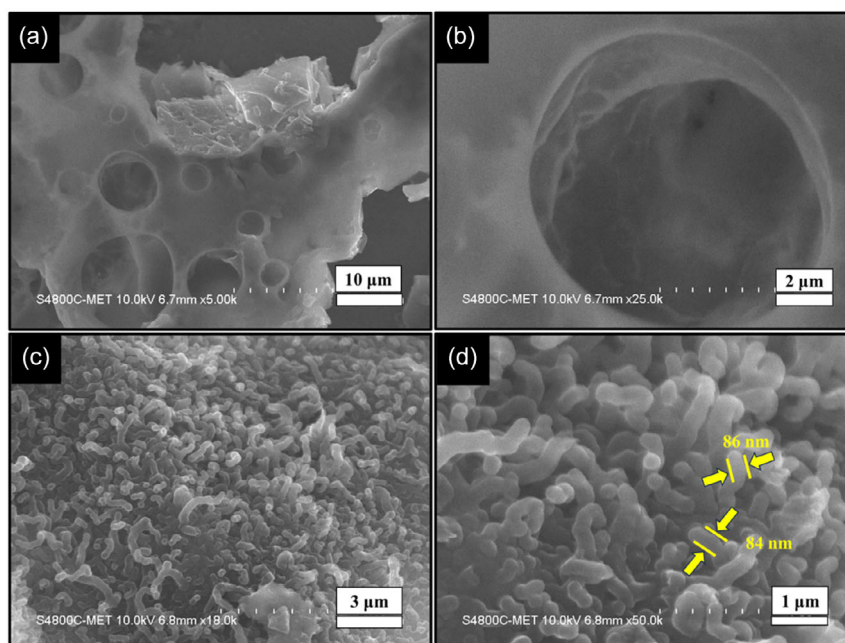
Figure 4 shows the FE-SEM images of the RP sample. Figure 4a,b confirms a highly disordered, porous structure characteristic of amorphous carbon formed due to the hot plasma treatment. The surface texture of amorphous carbon tends to be rough or uneven. Some image sections show thin carbon sheets, another characteristic of amorphous carbon. These sheets are often randomly arranged and loosely packed. The plasma treatment has induced the formation of numerous pores and voids, which significantly create abundant active sites for lithium-ion intercalation. Figure 4c,d shows the presence of typical carbon sheets with CNTs. The diameters of CNTs are ≈ 85 nm, demonstrating the thickness of CNTs and concluding the growth of MWCNTs. The surface of obtained CNTs is relatively smooth, suggesting structural defects. The CNTs that appeared in the sample are randomly oriented. The natural iron (Fe), manganese (Mn), and a minimal quantity of cobalt (Co) content in the biomass serve as an in-situ catalyst, simplifying the process by eliminating the need for additional catalysts.

The nanoparticles of Mn, Fe, and Co typically nucleate the growth of CNTs, where the size of these particles influences the diameter of the resulting CNTs.^[43] The thermal plasma method facilitated the rapid heating and carbonization of the biomass, resulting in the catalytic activity of Fe and the subsequent growth of CNTs. The size of Mn, Fe, and Co nanoparticles influences the diameter of the CNTs. Larger Mn, Fe, and Co particles tend to produce thicker CNTs, which might explain the relatively large diameter of the CNTs observed in the images. A smooth surface, as seen in the image, indicates good-quality CNTs with fewer defects. Defects would appear as irregularities, bends, or roughness along the tube surface.

3.6. FE-TEM

From Figure 5a, FE-TEM images reveal that the overall appearance suggests randomly oriented short and elongated CNTs dispersed within the carbon matrix with open ends. Open-ended CNTs typically appear darker near the edges in TEM images due to the increased electron density at the tube walls, which matches the dense, darker spots seen in this image. Figure 5b shows an MWCNT with a clear hollow center. The tube's walls are well-defined, indicating the presence of multiple graphitic layers. The CNT appears somewhat wavy and twisted. This could be due to the biomass-derived nature of the material and the growth conditions (high temperature in a plasma reactor), leading to a less ordered morphology than synthesized CNTs. The hollow core is a characteristic feature of CNTs, which is critical for ion transport in energy storage applications.

The CNT appears to have an approximate diameter of around 85 nm. CNTs in the image are curved and extend across the field of view; they appear to be different lengths. The CNTs in the image show clear, open structures where the tube's walls seem

**Figure 4.** a–d) FE-SEM images of the RP sample at different magnifications.

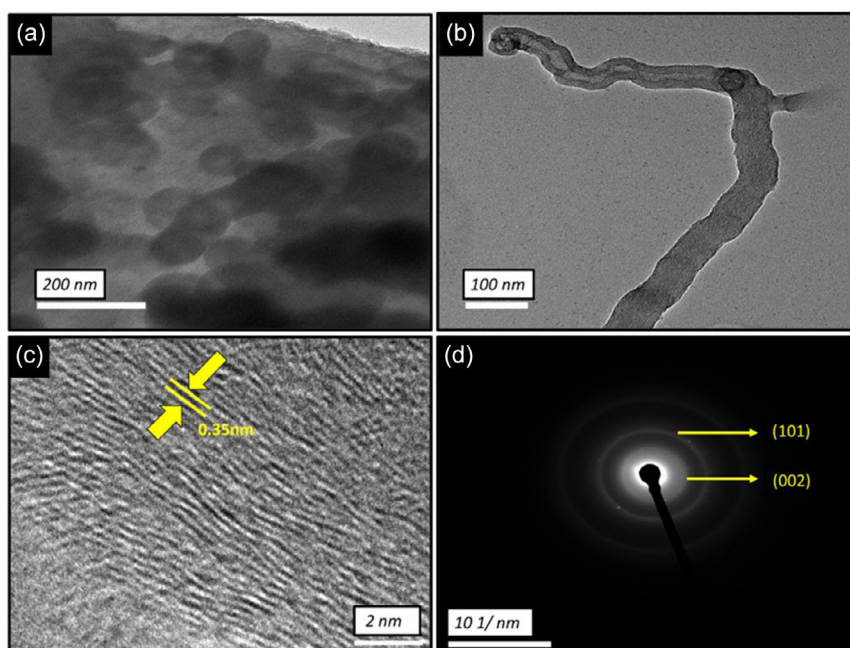


Figure 5. a,b) Low and high magnified TEM images, c) HRTEM, and d) SAED pattern of TEM images of the RP sample.

to terminate without any capping, indicating that this end of the CNTs is open. Open-ended CNTs allow easier access for Li^+ or Na^+ ions to enter and exit the hollow core, improving the intercalation process. This enhances the battery's charge/discharge efficiency. Also offers reduced resistance for ion transport into the tube, contributing to faster diffusion of ions.

The high-resolution TEM (HRTEM) image reveals the presence of crystalline graphitic carbon with an interlayer spacing of 0.35 nm (Figure 5c). The characteristic (002) plane of graphitic carbon is evident in Figure 5d. Furthermore, the (101) plane observed in the Selected area electron diffraction (SAED) pattern reflects in-plane crystalline ordering, confirming the presence of graphitic domains within the material. The coexistence of sharp diffraction rings, representing crystalline phases, and diffuse rings, indicative of amorphous structures, highlights the hybrid nature of graphitic CNTs and amorphous carbon phases.

4. Growth Mechanism of CNTs and Amorphous Carbon from Floral Biomass

The nucleation and growth of CNTs in biomass-derived carbon are heavily influenced by the presence of catalytic transition metals. In this study, Mn, Fe, and Co, naturally present in the RP flower biomass, acted as catalysts for CNT formation at high temperatures. Initial ICP analysis before the plasma treatment and acid leaching showed Mn, Fe, and Co concentrations around 6144.3, 1683.3, and 22.4 ppm, respectively, in the dried biomass sample. It is well known that Mn, Fe, and Co are the catalysts for the growth of CNTs. The minimal quantity of Co, about 22 ppm, shifted the focus to more of Mn and Fe, which are larger in quantity. Following acid leaching and subsequent plasma treatment,

the Mn and Fe concentration was reduced significantly to 10 and 87.2 ppm, respectively.

Both metals facilitate the dissociation of carbon-containing compounds under high-temperature conditions. With increasing carbon concentration, CNT nucleation occurs at the interface between Mn, Fe particles, and the carbon source. During growth, carbon atoms diffuse through or around the catalyst particle, precipitating on the opposite side to initiate tubular CNT structures. This process aligns with the base-growth mechanism, where the catalyst particle remains anchored to the substrate, while the CNT extends outward. As carbon atoms continue to precipitate, they arrange into hexagonal patterns, forming a continuous, graphitic cylinder-shaped tube on the catalyst surface. This results in the formation of graphitic, elongated CNT structures in the biomass-derived carbon material. Further, the H_2 evolution during the decomposition of biomass carbon reduced the amorphous nature of carbon and accelerated the growth of CNTs at high temperatures.^[44]

CNT growth continues as long as the catalyst remains active and dissolves and precipitates carbon atoms. Once the catalytic particles agglomerate or become encapsulated by a carbon layer, they become inactive, and CNT growth stops. However, in this case, Mn and Fe are not uniformly distributed and present in limited or localized areas. This uneven distribution of catalysts results in CNT growth being restricted to regions with sufficient concentrations to catalyze the reaction. In areas where catalysts are absent or below a threshold concentration, the catalytic process does not occur. This uneven distribution in the biomass leads to a mixed-phase carbon structure consisting of CNTs in the Fe-rich region. The localized presence of metals promotes the nucleation and growth of CNTs. These areas show graphitic, tubular carbon structures in the form of CNTs, which are typically observed in TEM and FE-SEM as long, tubular formations with varying

diameters. Carbon atoms fail to organize into well-ordered structures in regions with insufficient or absent catalysts. As a result, disordered carbon sheets or amorphous carbon are formed in these catalyst-deficient areas. A detailed tabulated comparison of the plasma-assisted synthesis method with conventional biomass-derived CNT synthesis techniques is provided in Table S1, Supporting Information.

5. Electrochemical Testing

5.1. LIB

EIS was performed to analyze the charge transfer and ion transport behavior of electrodes in LIBs. The Nyquist plots in Figure 6a showed a semicircle at high frequencies, corresponding to the charge transfer resistance (R_{ct}) at the electrode/electrolyte interface, coupled with a sloping line observed at low frequencies, which is indicative of ion diffusion processes within the electrode material. The measured R_{ct} value for Li was 47 Ω . The lower R_{ct} in LIBs indicates more efficient charge transfer, attributed to the high mobility of lithium ions and the improved electronic conductivity of the composite structure. After 3000 cycles, the R_{ct} increased to 97 Ω , doubling the initial value. This rise can be attributed to several factors, including the formation and thickening of the solid-electrolyte interphase (SEI) layer, reconstruction of the amorphous carbon and CNT network and increased impedance at the electrode-electrolyte interface due to

electrolyte decomposition over long-term cycling. The inset in Figure 6a shows the EIS-fitted equivalent circuit.

The CV was employed to assess the electrochemical properties of a biomass-derived carbon sample, configured as a half-cell with lithium foil as the counter electrode. The CV experiments were conducted at a scan rate of 0.1 V/s across a potential range of 0.01 to 3.0 V. The resulting CV curves for three cycles are presented in Figure 6b. The first cycle displays a significant reduction peak near 0.5 V, which signifies the initial lithiation of the carbon material. This process is essential for developing a SEI. The formation of the SEI is critical as it consumes lithium ions during the initial charging phase, resulting in irreversible capacity loss.^[45] Understanding this peak is crucial because it sheds light on the electrochemical behavior of the carbon material and the dynamics of SEI formation, both of which significantly influence the long-term cycling stability of LIBs. The energy consumed during the SEI formation contributes to the irreversible capacity loss observed in the first cycle.^[46]

In the second and third cycles, there is a noticeable stabilization in peak positions and current responses, indicating that the electrochemical behavior of the carbon material has become more consistent after the initial activation. The similarity between these cycles suggests that the carbon material shows enhanced cycling stability, which is an essential property for anode materials in LIBs.^[47] The current responses in these cycles confirm that the material is capable of reversible lithium intercalation and de-intercalation. This stability indicates that the initial SEI formation does not adversely affect the overall electrochemical

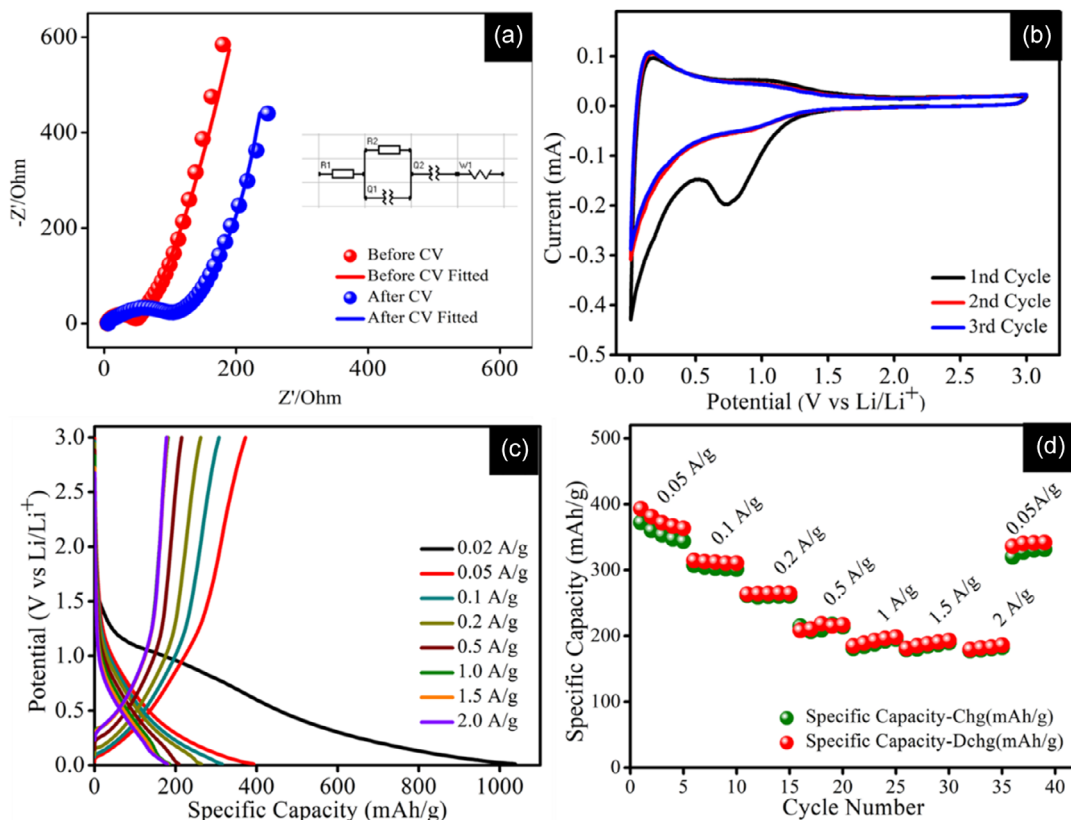


Figure 6. a) EIS (inset figure fitted circuit), b) CV, c) charge–discharge profiles at different current densities, and d) rate capability of RPLi coin cell.

performance of the electrode in later cycles.^[48] The broad redox peaks observed in the CV profile suggest that the carbon material exhibits mixed-phase characteristics. This behavior is often linked to the presence of both graphitic (CNT) and amorphous carbon structures, which can enhance the capacity for lithium-ion storage by providing varied electrochemical environments for lithium insertion.^[49] Additionally, a slight decrease in current density in the later cycles may reflect the establishment of a stable SEI layer. While this layer may initially lead to some capacity loss, it ultimately plays a vital role in improving long-term cycling performance by reducing further side reactions.^[50]

The charge–discharge profiles of the carbon anode (RLi cell) at varying current densities (0.02 to 2.0 A/g) are presented in Figure 6c. The first discharge at a low rate of 0.02 A/g exhibits a specific capacity exceeding 1000 mAh/g, but a notable drop to around 394 mAh/g occurs in the second cycle at 0.05 A/g. This reduction is attributed primarily to the formation of the SEI layer. In the initial cycle, lithium ions react irreversibly with the electrolyte, forming a passivating SEI layer on the carbon surface. This layer, essential for stabilizing the interface for future cycles, consumes lithium ions, which reduces the capacity available for subsequent cycling. The carbon material's high initial capacity also reflects lithium-ion interactions with defect sites, pores, and functional surface groups within the structure, which are more accessible in the first cycle. However, as these sites become saturated and the SEI layer stabilizes, they no longer contribute as significantly to capacity, resulting in the observed capacity reduction. The CV profile in Figure 5b also confirmed the same, with a reduction peak at 0.5 V, which is absent in subsequent cycles. As the current density increases from 0.1, 0.2, 0.5, 1, 1.5, to 2 A/g, the material retains stable capacities of 314, 263, 208, 185, 181, and 179 mAh/g, respectively, shown in Figure 6d. This capacity retention at high current rates suggests that the material supports efficient electron and ion transport, critical for high-rate applications. The combination of amorphous carbon and graphitic CNT phases within the material contributes significantly to this performance: The graphitic regions (CNTs) provide robust electron pathways, while the amorphous carbon phase supports flexible lithium storage. The rate capability, shown in Figure 6d, demonstrates that even after five cycles at each current density, the specific capacity at each current density remains stable, underscoring the anode's robust electrochemical

performance at high current densities, with excellent coulombic efficiency.

Furthermore, we conducted a comprehensive investigation into the long-term cycling performance of the RPLi cell represented in Figure 7. At high current rates of 0.5, 1.0, and 1.5 A/g. At 0.5 A/g (Figure 7a), we observed constant retention of specific capacity over 50 cycles, with a slight increase from 270 mAh/g to 290 mAh/g, achieving nearly 100% coulombic efficiency. The electrode demonstrated a relatively high specific capacity compared to the initial five cycles at 0.5 A/g, as shown in Figure 6d, which was around 210 mAh/g. A similar pattern of capacity increase with rising current density was observed at 1.0 A/g when compared to the first five cycles in Figure 6d. The specific capacity remained stable at 269 mAh/g after 50 cycles at this current rate, with a slight increase observed up to 276 mAh/g, maintaining almost 100% coulombic efficiency as per Figure 7a. To further evaluate the cycling stability performance of the electrode at an even high current rate of 1.5 A/g, it was subjected to testing over 3000 cycles. In Figure 7b, the initial specific capacity began at around 243 mAh/g and gradually increased to 318 mAh/g after 1000 cycles before declining to 287 mAh/g after 2000 cycles. Ultimately, on completion of 3000 cycles, the specific capacity was recorded at 233 mAh/g.

The exceptional performance of the RP sample is attributed to the unique structural features of the prepared material. A synergistic structure composed of CNTs with open ends confirmed by TEM images and disordered amorphous carbon with an interlayer spacing of 0.35 nm, indicating increased disorder within the carbon matrix. The open-ended CNTs provide direct pathways for lithium-ion intercalation, reducing ion diffusion resistance and enabling faster ion transport. Simultaneously, as per FE-SEM images, the amorphous carbon, formed during hot plasma treatment, exhibits a porous structure with numerous voids and surface defects, which significantly enhance the active sites for lithium-ion adsorption. This porous and disordered morphology improves electrolyte accessibility and facilitates rapid ion diffusion, particularly under high current densities. The combined effect of the open CNT ends expanded interlayer spacing in the disordered carbon, and the highly porous architecture is responsible for the material's superior electrochemical performance, particularly its high specific capacity and stability during long-term cycling at elevated current rates. A detailed tabulated

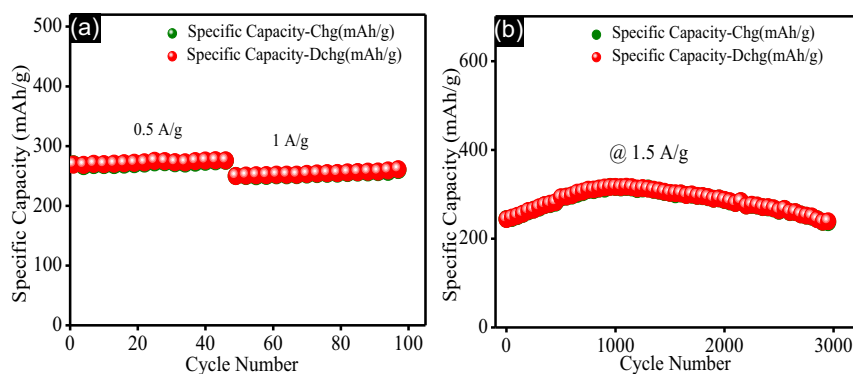


Figure 7. a) Cycling stability @ 0.5 and 1 A/g and b) cycling stability @ 1.5 A/g of RPLi.

comparison with previously reported work is provided in the Supporting Information in Table S2, Supporting Information.

5.2. SIB

Figure 8a demonstrates the EIS data for the NIB system. The semi-circle observed in the RPNa cell, the high-to-medium frequency range, corresponds to the charge-transfer resistance, measured at 230 Ω . The linear Warburg tail in the low-frequency region indicates ion diffusion behavior. The linear tail in the low-frequency region shows ion diffusion through the electrode. The inset Figure in Figure 8a shows the EIS-fitted equivalent circuit. The porous structure observed in FE-SEM images and the expanded interlayer spacing of 0.35 nm enhance Na-ion mobility, compensating for the higher charge-transfer resistance.

The CV measurements were carried out at a scan rate of 0.1 V/s within a potential window of 0.01 to 3.0 V. The initial cathodic sweep showed a broad reduction peak near 0.5–1.0 V (Figure 8b), corresponding to the formation of the SEI layer, which is a typical feature of carbon-based anodes. This irreversible process consumes sodium ions and leads to the initial capacity loss, as commonly observed in SIBs. A sharp peak near 0.01 V signifies the intercalation of sodium ions into the carbon matrix, indicating the presence of reversible sodium storage sites. In the second and third cycles, the cathodic and anodic peaks stabilized, with a reduction in the intensity of the SEI-related peak, suggesting a decrease in irreversible reactions. The anodic peaks between 0.2 and 0.5 V correspond to the deintercalation of sodium ions, confirming the reversible nature of the intercalation–deintercalation processes. The overlapping profiles of the second and third cycles highlight the material's stable electrochemical performance and minimal

degradation over initial cycling. The wide voltage window allowed the identification of both faradaic and nonfaradaic processes, with no significant peaks above 2 V, suggesting the dominance of electric double-layer capacitance (EDLC) in the absence of redox-active elements such as Fe. The smooth current response at higher voltages reinforces the amorphous carbon's role in contributing to capacitance through surface adsorption and desorption of sodium ions.

The charge–discharge profile of the SIB in Figure 8c demonstrates a strong dependence on current density, showcasing the material's response under varying rates. From Figure 8d, at a low rate of 0.02 A/g, the specific capacity reaches a high of 595 mAh/g, a value that is progressively reduced as the current density increases. By 0.05 A/g, the specific capacity drops to 212 mAh/g, reflecting the initial cycle activation and the saturation of active sites involved in sodium storage. This trend continues across the range of current densities, with capacities of 166, 122, 78, 46, and 30 mAh/g for current densities of 0.1, 0.2, 0.5, 1, and 1.5 A/g, respectively. The progressive decline in capacity at higher scan rates suggests that while the material supports moderate rates effectively, it experiences limitations in ion and electron transport at very high current densities. This outcome is consistent with SIB behaviors, as sodium ions, which are larger and slower-moving than lithium ions, experience greater difficulty diffusing into active sites in high-rate conditions.

The long-term cycling stability of this sodium-ion anode was further assessed at a high current rate of 0.5 A/g, where it exhibited remarkable stability over an extended test of 5000 cycles (Figure 8e). The specific capacity remained steady at around 75 mAh/g throughout the cycling period, with nearly 100% coulombic efficiency, underscoring the electrode's resilience and

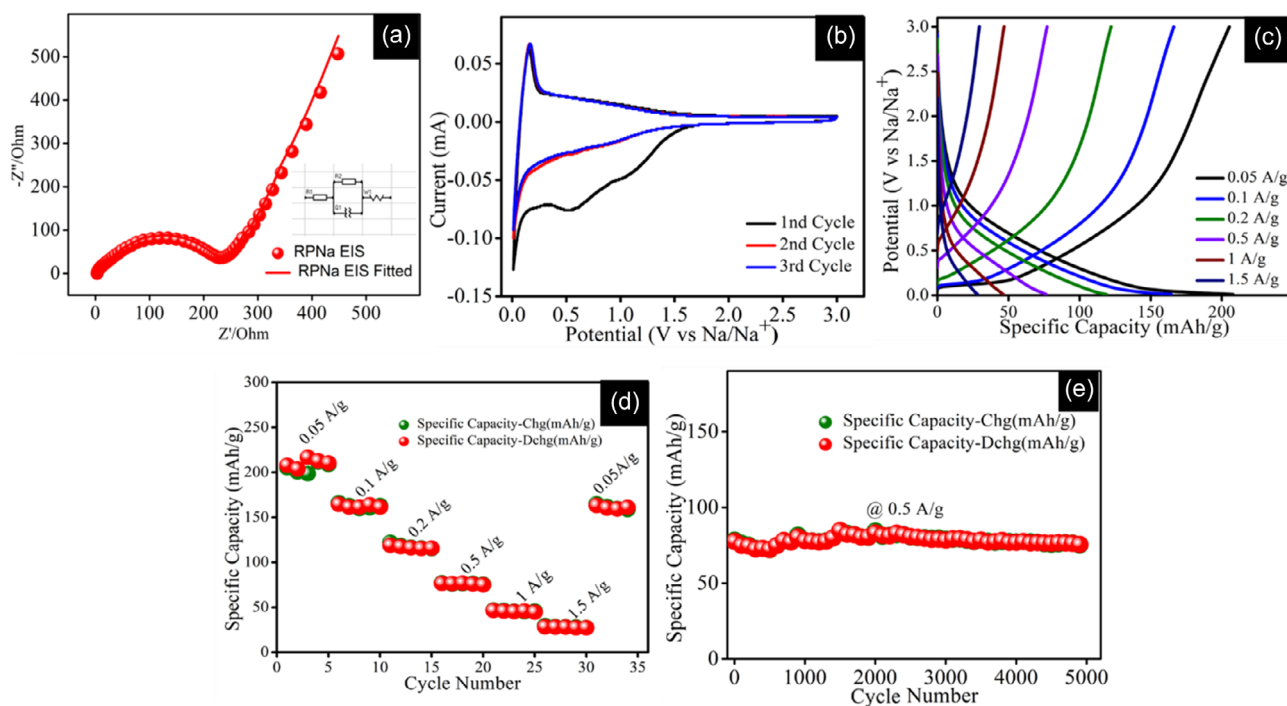


Figure 8. a) EIS (inset figure fitted circuit), b) CV, c) charge–discharge profiles at different current densities, d) rate capability, and e) cycling stability @0.5 A/g of RPNa.

efficient cycling at high rates. This stability at 0.5 A/g reflects a stable SEI layer, which prevents degradation of the electrode's structure and enables sustained sodium storage. The consistent performance, coupled with high coulombic efficiency, points to the anode's structural integrity and potential for long-life applications, making it a promising candidate for SIBs requiring long-term operation at moderate rates.

6. Conclusion

This study highlights the potential of biomass-derived carbon from RP flowers, synthesized through a high-temperature plasma process, as a versatile anode material for LIBs and SIBs. The carbon material obtained superior electrochemical performance stems from its unique structural features. The TEM analysis reveals the presence of open-ended CNTs with an interlayer spacing of 0.35 nm along with disordered amorphous carbon. The open-ended CNTs facilitate efficient lithium-ion intercalation, reducing diffusion resistance and enabling rapid ion transport, which is more adequate for high-current rate applications. The amorphous carbon exhibits a porous morphology with voids and surface defects, increasing active sites for ion adsorption and enhancing electrolyte accessibility. The combined effects of open CNT ends, expanded interlayer spacing, and a porous architecture result in a high initial specific capacity of over 394 mAh/g at 0.05 A/g and excellent stability, retaining 233 mAh/g after 3000 cycles at 1.5 A/g. For the SIB study, at a low rate of 0.02 A/g, the specific capacity reaches a high of 595 mAh/g. The long-term cycling stability of this sodium-ion anode was further assessed at a high current rate of 0.5 A/g, where it exhibited remarkable stability over an extended test of 5000 cycles. The specific capacity remained steady at around 75 mAh/g throughout the cycling period, with nearly 100% coulombic efficiency, demonstrating its adaptability for dual battery chemistry. Due to sustainability, efficient production, and remarkable cycling stability, the plasma-assisted synthesized carbon will be a promising candidate for next-generation energy storage systems.

Acknowledgements

The authors would like to thank the Baburaoji Gholap College, Centre for Materials for Electronics Technology (C-MET), MIT-World Peace University, Savitribai Phule Pune University, and Chimie des Interactions Plasma-Surface (ChIPS), Université de Mons for providing all research and characterization facilities. The authors would also like to thank the Ministry of Electronics and Information Technology (MeitY), Government of India, and Chhatrapati Shahu Maharaj Research, Training, and Human Development Organization (SARTHI) Maharashtra for financial support.

Conflict of Interest

The authors declare no conflict of interest.

Data Availability Statement

Research data are not shared.

Keywords: biomass carbon · carbon nanotubes · hot plasma · lithium-ion batteries · sodium-ion batteries

- [1] Y. Sun, S. Pal, M. K. Mahalik, G. Gozgor, C. K. M. Lau, *Energy Econ.* **2024**, *136*, 107735.
- [2] L. Pang, L. Liu, X. Zhou, M. Hafeez, S. Ullah, M. T. Sohail, *Energy Strategy Reviews* **2024**, *54*, 101460.
- [3] M. M. Mohideen, S. Ramakrishna, S. Prabu, Y. Liu, *J. Energy Chem.* **2021**, *59*, 688.
- [4] S. Afshan, I. Ozturk, T. Yaqoob, *Renew. Energy* **2022**, *196*, 151.
- [5] M. Yang, Y. Xie, Y. Zhu, Y. Mei, T. Zeng, D. Xie, D. Feng, *Ind. Eng. Chem. Res.* **2025**.
- [6] H. Li, X. Zhang, Z. Zhao, Z. Hu, X. Liu, G. Yu, *Energy Storage Mater.* **2020**, *26*, 83.
- [7] C. Wu, Y. Yang, Y. Zhang, H. Xu, X. He, X. Wu, S. Chou, *Chem. Sci.* **2024**, *15*, 6244.
- [8] M. S. Soffian, F. Z. Abdul Halim, F. Aziz, M. A. Rahman, M. A. Mohamed Amin, D. N. Awang Chee, *Environ. Adv.* **2022**, *9*, 100259.
- [9] T. Temesgen, E. T. Bekele, B. A. Gonfa, L. T. Tufa, F. K. Sabir, S. Tadesse, Y. Dessie, *J. Energy Storage* **2023**, *73*, 109293.
- [10] Y. Ma, D. Yao, H. Liang, J. Yin, Y. Xia, K. Zuo, Y. P. Zeng, *Ultra-thick wood biochar monoliths with hierarchically porous structure from cotton rose for electrochemical capacitor electrodes* **2020**.
- [11] B. Liu, M. Yang, H. Chen, Y. Liu, D. Yang, H. Li, *J. Power Sources* **2018**, *397*, 1.
- [12] Y. Zhan, H. Zhou, F. Guo, B. Tian, S. Du, Y. Dong, L. Qian, *J. Energy Storage* **2021**, *34*, 102180.
- [13] T. Zhang, J. Mao, X. Liu, M. Xuan, K. Bi, X. L. Zhang, J. Hu, J. Fan, S. Chen, G. Shao, *RSC Adv.* **2017**, *7*, 41504.
- [14] B. Ma, Y. Huang, Z. Nie, X. Qiu, D. Su, G. Wang, J. Yuan, X. Xie, Z. Wu, *RSC Adv.* **2019**, *9*, 20424.
- [15] R. M. Bhattarai, K. Chhetri, S. Natarajan, S. Saud, S. J. Kim, Y. S. Mok, *Chemosphere* **2022**, *303*, 135290.
- [16] K. Wang, Y. Jin, S. Sun, Y. Huang, J. Peng, J. Luo, Q. Zhang, Y. Qiu, C. Fang, J. Han, *ACS Omega* **2017**, *2*, 1687.
- [17] N. Zhang, Q. Liu, W. Chen, M. Wan, X. Li, L. Wang, L. Xue, W. Zhang, *J. Power Sources* **2018**, *378*, 331.
- [18] B. Said, O. Bacha, Y. Rahmani, N. Harfouche, H. Kheniche, D. Zerrouki, H. Belkhalifa, A. Henni, *Inorg. Chem. Commun.* **2023**, *155*, 111012.
- [19] E. Taer, D. Afdal Yusra, A. Amri, R. Awitdrus Taslim, Apriwandi Agustino, A. Putri, *The Synthesis Of Activated Carbon Made From Banana Stem Fibers As The Supercapacitor Electrodes*, In: *Mater Today Proc*, Elsevier Ltd **2020**, pp. 3346–3349. <https://doi.org/10.1016/j.matpr.2020.11.645>.
- [20] L. Wan, D. Chen, J. Liu, Y. Zhang, J. Chen, C. Du, M. Xie, *J. Alloys. Compd.* **2020**, *823*.
- [21] B. K. Saikia, S. M. Benoy, M. Bora, J. Tamuly, M. Pandey, D. Bhattacharya, *Fuel* **2020**, *282*, 118796.
- [22] L. Ge, M. Zuo, Y. Wang, R. Wang, N. Rong, Z. Qi, C. Zhao, Y. Zhang, C. Xu, *J. Anal. Appl. Pyrolysis* **2024**, *177*, 106320.
- [23] G. P. Gakis, S. Termine, A.-F. A. Trompeta, I. G. Aviziotis, C. A. Charitidis, *Chem. Eng. J.* **2022**, *445*, 136807.
- [24] N. P. D. Ngidi, A. F. Koekemoer, S. S. Ndlela, *Phys. Chem. Earth. Parts A/B/C* **2024**, *135*, 103698.
- [25] Y. Yu, Y. Wang, F. Yang, D. Feng, M. Yang, P.-F. Xie, Y. Zhu, M. Shao, Y. Mei, J.-C. Li, *Angew. Chem., Int. Ed.* **2025**, *64*, e202415691.
- [26] K. Kumar, R. Kumar, S. Kaushal, N. Thakur, A. Umar, S. Akbar, A. A. Ibrahim, S. Baskoutas, *Chemosphere* **2023**, *345*, 140419.
- [27] S. A. Raut, N. S. Kanhe, S. V. Bhoraskar, A. K. Das, V. L. Mathe, *J. Appl. Phys.* **2014**, *116*.
- [28] N. S. Kanhe, A. K. Tak, A. B. Nawale, S. A. Raut, S. V. Bhoraskar, A. K. Das, V. L. Mathe, *Mater. Des.* **2016**, *112*, 495.
- [29] N. S. Kanhe, A. Kumar, S. M. Yusuf, A. B. Nawale, S. S. Gaikwad, S. A. Raut, S. V. Bhoraskar, S. Y. Wu, A. K. Das, V. L. Mathe, *J. Alloys Compd.* **2016**, *663*, 30.
- [30] S. A. Raut, P. R. Mutadak, S. Kumar, N. S. Kanhe, S. Huprikar, H. V. Pol, D. M. Phase, S. V. Bhoraskar, V. L. Mathe, *J. Magn. Magn. Mater.* **2018**, *449*, 232.
- [31] S. M. Lee, S. H. Lee, J. S. Roh, *Crystals Basel* **2021**, *11*, 1.

- [32] S.-H. Yeon, C.-S. Jin, K.-H. Shin, S. Hwang, M.-S. Jeon, S.-K. Park, D. H. Kim, S.-O. Kim, S. S. Jang, *In MAX-Derived Carbon Anode During Cycling*, Carbon, NY 185 **2021** 681.
- [33] D. Kong, Z. Xiao, Y. Gao, X. Zhang, R. Guo, X. Huang, X. Li, L. Zhi, *Mater. Sci. Eng., R: Reports* **2019**, 137, 1.
- [34] K. Yun, G. Yoo, S.-O. Kang, S.-S. Chee, S. Yang, G.-H. An, *ACS. Sustain. Chem. Eng.* **2024**, 12, 16229.
- [35] E. Picheau, A. Impellizzeri, D. Rybkovskiy, M. Bayle, J.-Y. Mevellec, F. Hof, H. Saadaoui, L. Noé, A. C. Torres Dias, J.-L. Duvail, M. Monthieux, B. Humbert, P. Puech, C. P. Ewels, A. Pénicaud, *ACS Nano* **2021**, 15, 596.
- [36] S. Chaunchaiyakul, T. Yano, K. Khoklang, P. Krukowski, M. Akai-Kasaya, A. Saito, Y. Kuwahara, *Nanoscale analysis of multiwalled carbon nanotube by tip-enhanced Raman spectroscopy*, Carbon, NY 99 **2016** 642–648.
- [37] P. Konnerth, D. Jung, J. W. Straten, K. Raffelt, A. Kruse, *Energy Technol.* **2021**, 4, 69.
- [38] J. Deng, T. Xiong, F. Xu, M. Li, C. Han, Y. Gong, H. Wang, Y. Wang, *Green Chem.* **2015**, 17, 4053.
- [39] Y. Yuan, Y. Sun, Z. Feng, X. Li, R. Yi, W. Sun, C. Zhao, L. Yang, *Materials* **2021**, 14, 318.
- [40] V. Datsyuk, M. Kalyva, K. Papagelis, J. Parthenios, D. Tasis, A. Siokou, I. Kallitsis, C. Galiotis, *Chemical oxidation of multiwalled carbon nanotubes*, Carbon, NY 46 **2008** 833–840.
- [41] A. Ganguly, S. Sharma, P. Papakonstantinou, J. Hamilton, *J. Phys. Chem. C* **2011**, 115, 17009.
- [42] M. Jahan, F. Feni, *Adv. Mater. Phys. Chem.* **2022**, 12, 106.
- [43] J.-P. Tessonier, D. S. Su, *ChemSusChem* **2011**, 4, 824.
- [44] S. Pinjari, M. K. Kumaravelan, V. C. Peddy, S. Gandham, J. Patruni, S. Velluru, P. Kumar, *Int. J. Hydrogen Energy* **2018**, 43, 2781.
- [45] Y. X. Lin, Z. Liu, K. Leung, L. Q. Chen, P. Lu, Y. Qi, *J. Power Sources* **2016**, 309, 221.
- [46] X. Li, X. Sun, X. Hu, F. Fan, S. Cai, C. Zheng, G. D. Stucky, *Nano. Energy* **2020**, 77, 105143.
- [47] X. Qu, G. Huang, B. Xing, D. Si, B. Xu, Z. Chen, C. Zhang, Y. Cao, *J. Alloys Compd.* **2019**, 772, 814.
- [48] Y. Rangom, R. R. Gaddam, T. T. Duignan, X. S. Zhao, *ACS Appl. Mater. Interfaces* **2019**, 11, 34796.
- [49] H. Geng, Y. Peng, L. Qu, H. Zhang, M. Wu, *Adv. Energy Mater.* **2020**, 10, 1.
- [50] J. Li, A. Manthiram, *Adv. Energy Mater.* **2019**, 9, 1.

Manuscript received: March 19, 2025
Revised manuscript received: May 14, 2025
Version of record online: